Monolithic Multi-Element HPGe Detector Equipped With CMOS Preamplifiers: Construction and Characterization of a Demonstrator

Nicola Tartoni, *Member, IEEE*,
R. Crook, T. Krings, D. Protić, C. Ross, L. Bombelli, R. Alberti, T. Frizzi, and V. Astromskas

***Abstract*—Multi-element germanium detectors for X-ray fluorescence are widely used in synchrotron experiments and in particular in XAFS experiments. This paper presents the construction and characterization of a demonstrator built to investigate the viability of multi-element monolithic germanium detectors equipped with CMOS front-end electronics. Semikon Detector GmbH fabricated a germanium sensor segmented with a pad pattern with pad size 1×1 mm^2. 16 channels were instrumented with the CUBE preamplifiers developed at XGLab Srl. The detector was tested with radioactive sources and with the synchrotron X-ray beam of Diamond. The results showed spectra with energy resolution satisfactory for XAFS experiments but with a considerable tail. The low energy tail was proved to be due to charge sharing. In addition the spectra showed the peak stability as a function of counting rate better than 1% for rate up to 838 kcps. The non-linearity of the peak position vs. energy was estimated to be a maximum of 0.13% No evidence of charge loss in the crystal was identified. This work proved that this technology is a viable option to improve the throughput of germanium fluorescence detectors as long as methods to reduce events leading to charge sharing are in place.**

***Index Terms*—Semiconductor radiation detectors, X-ray detectors.**

I. Introduction

X-RAY ABSORPTION FINE STRUCTURE (XAFS) experiments are a class of experiments routinely performed at synchrotron radiation facilities and broadly used in diverse fields of science such as chemistry, biology, environmental science, material science, and others. XAFS is a powerful and versatile technique for studying structures of materials [1]. Due to the nature of the technique, it can be applied to crystalline and amorphous compounds, and to solid, liquid or even gaseous materials.

Manuscript received May 08, 2014; revised August 01, 2014; accepted November 20, 2014. Date of publication January 26, 2015; date of current version February 06, 2015.

N. Tartoni and R. Crook are with Diamond Light Source Ltd., Didcot, Oxfordshire OX14 3XH, U.K. (e-mail: nicola.tartoni@diamond.ac.uk; robert.crook@diamond.ac.uk).

T. Krings, D. Protić, and C. Ross are with Semikon Detector GmbH, D-52425 Jülich, Germany (e-mail: info@semikon-detector.de).

L. Bombelli, R. Alberti, and T. Frizzi are with XGLab Srl, Milan 20133, Italy (e-mail: bombelli@xglab.it; alberti@xglab.it; frizzi@xglab.it).

V. Astromskas is with the University of Surrey, Guildford GU2 7XH, U.K. and also with Diamond Light Source Ltd., Didcot, Oxfordshire OX14 3XH, U.K. (e-mail: v.astromskas@surrey.ac.uk).

Digital Object Identifier 10.1109/TNS.2014.2381492

When studying dilute samples, the absorption coefficient is obtained by measuring the variation of the intensity of the fluorescence emitted by the element under study. In this experimental condition the majority of the radiation coming from the sample is elastically scattered radiation that carries no information. The angular dependence of the elastically scattered radiation [2], [3] and the polarization properties of synchrotron radiation [4] show that the line of view minimizing the scattering is normal to the incident radiation beam and lying in the plane of the orbit of the electrons.

The above mentioned facts set the requirements of fluorescence detectors for XAFS experiments. They need to have the energy resolution good enough to separate fluorescence radiation from elastically scattered radiation (250 eV FWHM at 6 keV is generally considered good enough). They need to have high throughput in order to detect as many photons as possible. The throughput is increased by building multi-element detectors. However when the elements are located too far from the ideal line of view the fluorescence radiation is overwhelmed by the elastically scattered radiation and therefore these elements become useless. Just to fix some numbers we can note that because of the angular dependency of the elastic cross section [2], [3] the intensity of the elastically scattered radiation in the plane of the orbit at a scattering angle of 100° is 4 times its intensity at a scattering angle of 95°. The situation is further exacerbated when moving off the plane of the orbit. So the compactness of the detector is a requirement as important as the others and this is the reason why monolithic multi-element detectors have been developed [5].

An additional requirement is that the detector must not introduce artifacts such as the escape peak of the elastically scattered radiation (much more intense than fluorescence) overlapping with the fluorescence peak under study or fluorescence from materials inside the detector being excited and resulting in spurious features in the spectrum. For this reason germanium detectors, whose K_α escape peak is about 9.9 keV below the main peak, are preferred to silicon detectors whose K_α escape peak is about 1.7 keV below the main peak and then can interfere with the fluorescence of elements such as selenium. Finally the relatively thin silicon drift detectors are not optimal for use in XAFS experiments as a considerable fraction of radiation goes through them and can then excite fluorescence from the materials of the electronic interconnections behind the detector leading to spurious features in the spectrum.

Diamond Light Source has in operation state-of-the-art multi-element monolithic HPGe detectors with JFETs as front-end electronic components, the largest of them is installed in the beam line I20 [6]. The beam line I20 can operate at a photon energy that goes from 4 keV to 19 keV with a crystal monochromator using Si(111) and from 7 keV to 34 keV using Si(311). The radiation source of the beam line I20 is a wiggler giving a very high photon flux, up to 5×10^{12} photons per second at 10 keV with Si(111). The detector of I20 has 64 elements arranged as a pad pattern on an electrode of a single germanium crystal. The pads are square with 5 mm sides and they are arranged in a matrix of 8×8 pads. A collimator preventing X-rays from landing at the boundary of the pads improves the peak to valley ratio of the spectra produced by the detector.

The samples measured in XAFS experiments are very diverse and the photon flux reaching the detector depends a lot on the sample under study. The throughput could be increased by increasing the number of elements. However at a typical distance of the detector from the sample of 250 mm and with the centre of the detector at 90° with respect to the line of flight the outer pads are approximately located between 94° and 96° and adding elements would lead them further off the axis. The detector can be moved further back from the sample but there are practical limits to how far it is possible to go. A possible way to increase the number of channels without increasing the scattering angle is then to shrink the pad size. The purpose and main motivation of this work is then to investigate if the miniaturization of germanium detectors for XAFS experiment is viable.

In recent years integrated charge sensitive preamplifiers, known with the commercial name of "CUBE", have been developed by XGLAB Srl [7], [8]. These preamplifiers were developed to be used with silicon drift detectors, however they could provide an effective path to the miniaturization of germanium detectors. A demonstrator of this technology was built in collaboration with Semikon Detector GmbH, a manufacturer of position-sensitive germanium and silicon lithium drifted detectors, and XGLab Srl. In this paper we report the details of the construction of this demonstrator, its characterization done with radioactive sources and with synchrotron radiation X-ray beam.

II. Demonstrator Construction

A. Ge Detector Fabrication

The detector was fabricated using a germanium crystal whose size was 20 mm $\times$ 20 mm and 4 mm thick. The front face of the crystal was boron implanted to create a continuous p+ contact. The rear face was phosphor implanted to create an n+ contact. This n+ contact was structured - using a mask that the manufacturer had used previously - as a 10×10 matrix of square pads. The size of each pad is 1 mm $\times$ 1 mm. The pads are isolated by plasma-etched grooves [9] that are approximately 40 μm wide and 15 μm deep. The matrix is surrounded by guard structures. A segmented sensor with 100 channels and 1 cm^2 of sensitive area was then obtained. The full depletion voltage provided by the manufacturer for this device is 80 V.

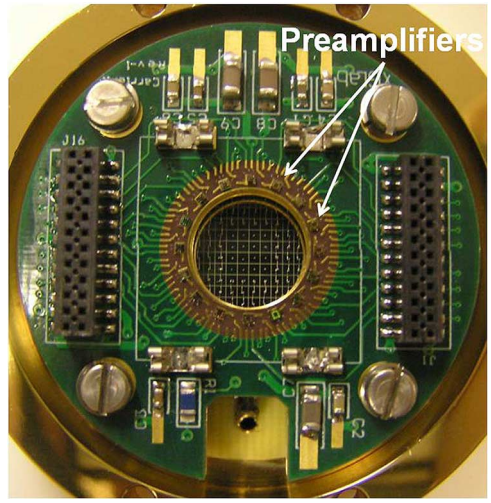

Fig. 1. The carrier printed circuit board with the 16 preamplifiers on the edge of the central hole that enables them to be wire bonded to the detector underneath. The side of the pads of the germanium detector, visible through the hole in the printed circuit board, is 1 mm and provides the scale of this picture. The arrangement is very compact.

The detector so fabricated is exposed to X-rays from the continuous electrode side and the charge is collected from the structured electrode side. The thickness of the boron implant is less than 1 μm, 250 nm of aluminum are deposited on the top of the boron implanted surface to create the electrical contact. As a result over 91% of 6 keV photons go through the aluminum metallization and boron implant [10].

B. Front-End Electronics

In order to keep the cost of our demonstrator within the budget and to prevent it from becoming excessively complex only the 16 central pads were connected to preamplifiers by wire bonding. The remaining pads were connected by wire bonding to the guard ring. This in turn was connected to the crystal holder which is at the ground potential. The preamplifiers are hosted by a carrier printed circuit board (CPCB) with a central hole and located on the edge of the hole. The CPCB is installed just above the germanium crystal and the wire bonding goes through the hole in the printed circuit board. Fig. 1 shows the CPCB above the crystal and highlights the compactness that can be achieved with integrated preamplifiers.

The CPCB routes the power supply tracks, the reset logic signals, and the analogue output of the preamplifiers from and to the connectors on the periphery of the board. The ground potential of the board is connected to the crystal holder.

The integrated charge-sensitive preamplifiers are built with CMOS technology. The input device of the preamplifiers is a PMOSFET. The higher flicker noise of PMOSFETs with respect to JFETs is compensated by low input capacitance and high transconductance [11], [12]. Thus integrated charge preamplifiers manage to achieve signal to noise ratios high enough to be used in spectroscopy grade detectors. The preamplifiers that we used have a feedback capacitance of 25 fF and the charge sensitive stage is followed by a gain stage with a gain of 3.5. The preamplifiers are operated in pulse reset mode. When the

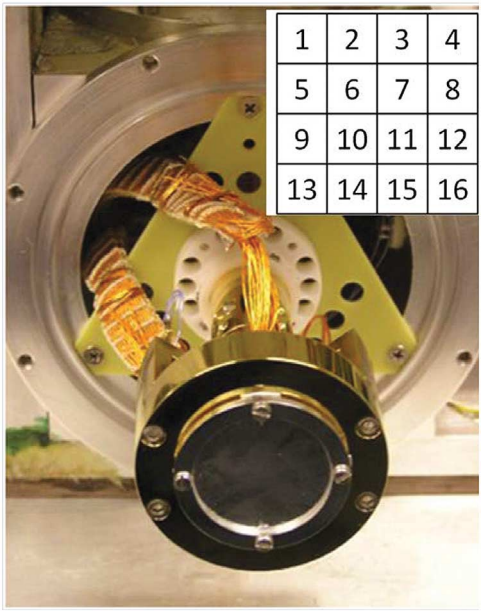

Fig. 2. The crystal holder mounted in the cryostat with an aluminum foil 10 μm thick acting as infrared radiation shield. The orange flat cables are the kapton insulated cables connecting the CPCB to the feedthroughs on the rear flange. The diagram shows the correspondence between channels and pads as the crystal is seen from the entrance window.

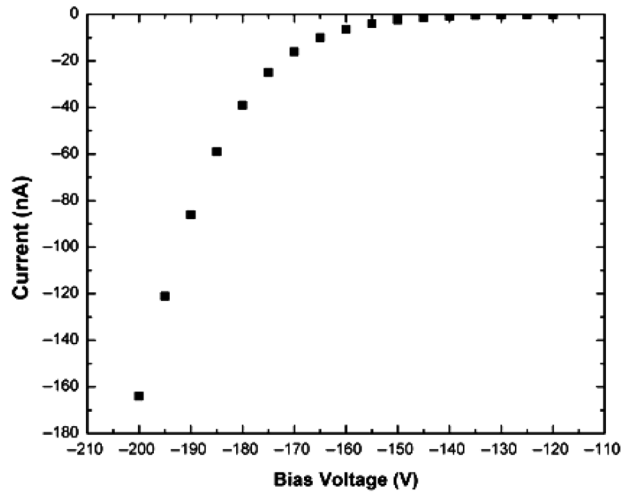

Fig. 3. Reversed bias I-V characteristic curve of the detector.

preamplifier output achieves a predetermined level some ancillary electronics trigger the reset of that preamplifier. The reset rate depends then on the counting rate; however the reset rate does not affect the performance of the preamplifiers.

Two different versions of preamplifiers were installed in this demonstrator. The standard version has the possibility of tuning the supply voltages through its associated electronics while the other version, a new prototype, does not have this feature. However the new prototype has the advantage of requiring a smaller number of bonding pins.

C. Mounting of the Detector in the Cryostat and Ancillary Electronics

The limitation in the amount of channels enabled the use of an old cryostat after an appropriate refurbishment. A crystal holder was specifically designed for this project and installed in the cryostat. Fig. 2 shows the crystal holder mounted on the cryostat with the diagram of the correspondence between the channel number and pad on the crystal as seen from the entrance window.

The detector is behind an aluminum foil 10 μm thick acting as infrared radiation shield. The CPCB is connected to feedthroughs present on the rear flange by kapton insulated flat cables visible in Fig. 2.

On the exterior of the cryostat are located two printed circuit boards that provide the reset logic signals for the preamplifiers. Each board routes the analogue signal of 8 preamplifiers to 8 SMA connectors. In addition the boards route and filter the power supply for the preamplifiers. The preamplifiers can be reset independently or simultaneously by appropriately setting some jumpers on the boards. These jumpers enable also to select any preamplifier that is desired to be kept inactive.

The ground potential of power supply lines, reset logic signals, and analogue signals in the CPCB and in the external printed circuit boards are connected by dedicated wires.

The bias voltage for the crystal is provided by an external bias supply connected by an SHV vacuum feedthrough that is mounted on the rear flange. A filter made out of a bias resistor of 1 MOhm and a shunt capacitor of 100 nF located in a die-cast box between the SHV connector and the bias supply provide appropriate filtering of the bias voltage. The ground potential of the high voltage bias supply is connected to the crystal holder.

III. Test Results

A. Electrical Tests

A measurement of the current-voltage (I-V) characteristic and some analysis on the output waveforms of the preamplifiers were performed with the detector at low temperature.

The I-V characteristic was measured with a Keithley 2410 applying the voltage through the SHV connector. The characteristic curve was measured with the voltage down to -200 V is shown in Fig. 3. The current that was measured at -200V of bias was 164 nA. The operating voltage of the detector was chosen to be -180 V where the reverse current was 39 nA.

The bulk component for each pad can be calculated by measuring the slope of the preamplifier output due to dark current only (detector not irradiated). When operating at -180V the slopes of the channels are measured to be between 2 V/s and 4 V/s. From the parameters of the preamplifier (see Section II-B) it is calculated that the reverse current for each pad is between 14 fA and 29 fA leading to a maximum of about 3 pA for the reverse current of the entire matrix of 100 elements. Comparing this current value with the value measured, the majority of the reverse current is due to a component going through the edge of the crystal into the guard ring.

The channels related to the central pads (6, 7, 10, and 11) show better noise performance with respect to the others. This was attributed to the fact that each preamplifier keeps the voltage of the input node at about 1 V. Since the pads that are not equipped with preamplifiers are grounded (0 V)

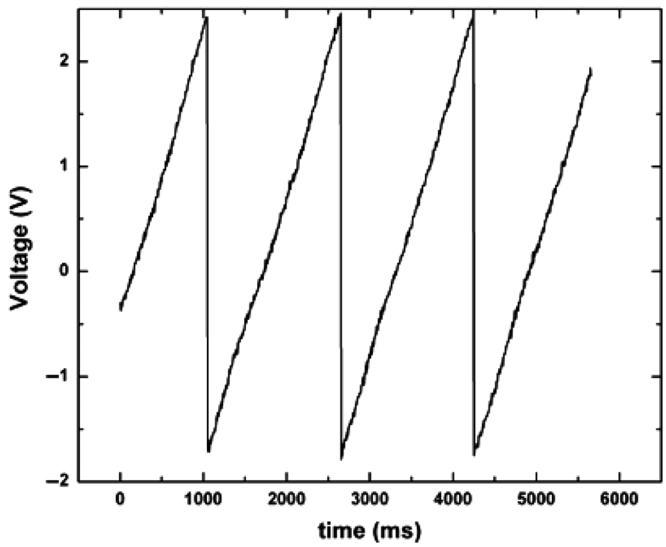

Fig. 4. Output voltage of the channel 7 preamplifier when the detector is not irradiated.

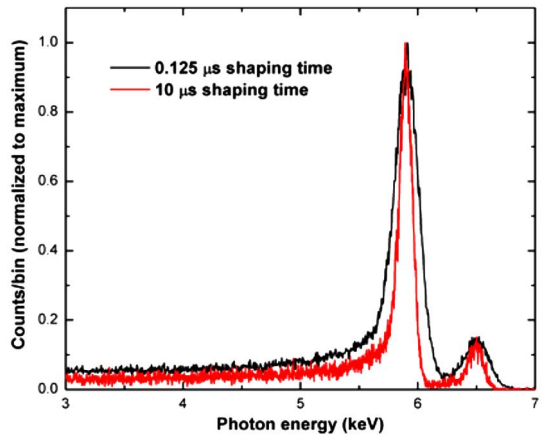

Fig. 5. Spectra of ^{55}Fe normalized to the maxima at shaping time of 0.125 μs (black line) and 10 μs (red line) acquired from channel 11.

it means that there is a potential difference between the outer instrumented pads and their grounded neighbours. This leads to extra leakage current between those pads and then to higher noise with respect to the central ones. The tests with radioactive sources were then performed on the central channels only. Since the channels 6, 7, 10, and 11 perform very similarly, all the measurements reported in the graphs related to one channel represent the other three. Fig. 4 shows the output waveform of channel 7.

Finally the scope tracks reveal cross talk between channels during the reset. This feature was not visible when the board was tested on the bench before it was wire-bonded to the pads. The cross talk is then due to the inter-capacitance between pads.

B. Tests with ^{55}Fe Radioactive Source

The tests with radioactive sources were carried out by connecting the output of the preamplifiers to standard off-the-shelf shaping amplifiers and then acquiring the spectra with a multichannel analyzer. Two different shaping amplifiers were used, Ortec 671 and Canberra 2016 A, and a multichannel analyzer Ortec Aspec-927. The two amplifiers enabled to span a shaping time range from 10 μs to 0.125 μs. Spectra from an ^{55}Fe radioactive source, that emits Mn characteristic X-rays, were acquired for the four central channels and for the entire range of shaping times offered by the two shaping amplifiers used. Two examples of such spectra for channel 11 are shown in Fig. 5 for 10 μs and 0.125 μs shaping time. The spectra were acquired at a counting rate of approximately 2×10^3 counts per second. The energy resolution is satisfactory because the Mn K_α and K_β peaks appear well separated but at the same time a considerable tail at photon energies smaller than the energy of the peaks is present. The origin of the tail is investigated in the tests with synchrotron radiation described in the next section.

In order to extract quantitative information from the data an analytical model was used to fit the experimental spectra from ^{55}Fe. The model that we used is a modification of models used in the past for fitting peaks from germanium detectors [13]. Each peak is modeled by a Gaussian function summed to two exponential functions and a constant. Both the exponential functions and the constant are multiplied by functions that bring them quickly to zero for channels higher than the Gaussian centroid value. Spectra from ^{55}Fe are then represented by the sum of two such functions modeling the overlapping Mn K_α and K_β peaks. We have then the following analytical expression:

$$
\begin{aligned}
&A \cdot e^{-\frac{(X_a - x)^2}{2\cdot\sigma_a^2}} + B \cdot e^{-\frac{(X_b - x)^2}{2\cdot\sigma_b^2}} \\
&\quad + b_s \cdot A \cdot e^{\frac{(x - X_a)}{P1_s}} \cdot \left[1 - \operatorname{erf}\left(\frac{(x - X_a)}{P2_s * \sigma_a \cdot \sqrt{2}} + \frac{P2_s * \sigma_a}{P1_s \cdot \sqrt{2}}\right)\right] \\
&\quad + b_l \cdot A \cdot e^{\frac{(x - X_a)}{P1_l}} \cdot \left[1 - \operatorname{erf}\left(\frac{(x - X_a)}{P2_l * \sigma_a \cdot \sqrt{2}} + \frac{P2_l * \sigma_a}{P1_l \cdot \sqrt{2}}\right)\right] \\
&\quad + b_s \cdot B \cdot e^{\frac{(x - X_b)}{P1_s}} \cdot \left[1 - \operatorname{erf}\left(\frac{(x - X_b)}{P2_s * \sigma_b \cdot \sqrt{2}} + \frac{P2_s * \sigma_b}{P1_s \cdot \sqrt{2}}\right)\right] \\
&\quad + b_l \cdot B \cdot e^{\frac{(x - X_b)}{P1_l}} \cdot \left[1 - \operatorname{erf}\left(\frac{(x - X_b)}{P2_l * \sigma_b \cdot \sqrt{2}} + \frac{P2_l * \sigma_b}{P1_l \cdot \sqrt{2}}\right)\right] \\
&\quad + \frac{c \cdot A}{\left[1 + e^{\frac{(x - X_a)}{0.75 \cdot \sigma_a}}\right]} + \frac{c \cdot B}{\left[1 + e^{\frac{(x - X_b)}{0.75 \cdot \sigma_b}}\right]}
\end{aligned}
$$

X_a and X_b are the centroid of the two Gaussian functions and σ_a and σ_b their standard deviations. The tails are modeled by the exponential functions where $P1_l$ and $P1_s$ are the decaying constants of the tail. The amplitude of the exponential functions is proportional to the amplitude of the Gaussian functions with proportionality constant b_l and b_s. $P2_l$ and $P2_s$ are parameters that measure how fast the function go to zero after the centroid of the Gaussian function (erf is the error function). Finally c is the fraction of the Gaussian amplitude contributing to the constant. The exponential function at the denominator of the constant contribution brings this contribution to the spectrum to zero after the centroid of the Gaussian function. Fig. 6 shows the ^{55}Fe from channel 10 at 10 μs shaping time with the fitted function superimposed to the data measured. The FWHM of the Gaussian components of the K_α peaks are reported in the graph in Fig. 7.

The FWHMs of the peaks measured empirically (measuring just the width at the half maximum of the peak and disregarding

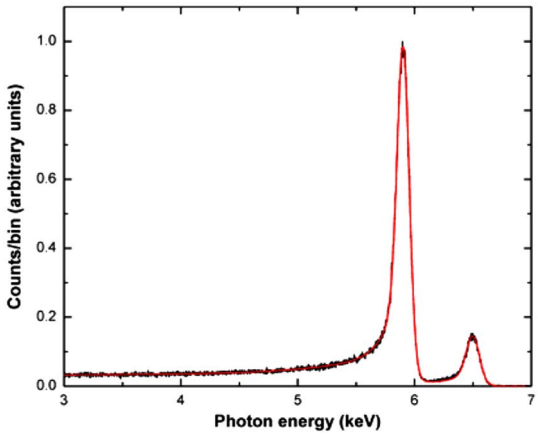

Fig. 6. Spectrum of ^{55}Fe normalized to maximum (black line) acquired from channel 10 at shaping time of 10 μs with the fitted function (red line) superimposed to the experimental data.

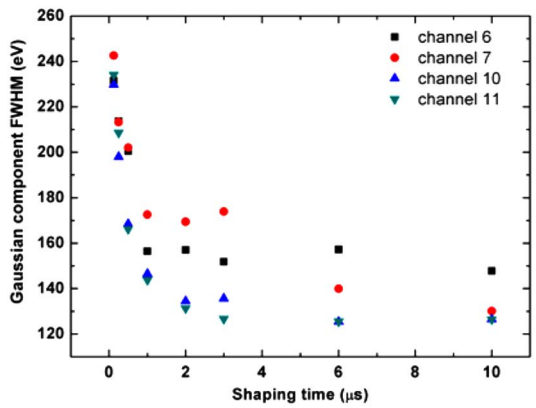

Fig. 7. Gaussian peak width (FWHM in eV) of the spectra measured by the channels 6, 7, 10, and 11 for semi-gaussian shaping times of 10, 6, 3, 2, 1, 0.5, 0.25, and 0.125 μs. These values are for the K_α peaks.

any other characteristics) are approximately 15% larger than the FWHM of the Gaussian component of our model that is the first term of the equation. The other terms of the equation (the tail components) lead to the broadening of the peak that is measured empirically.

C. Tests with ^{241} Am and ^{57}Co Radioactive Sources

Tests with ^{241}Am and ^{57}Co have also been performed and the results show the same qualitative characteristics of the ^{55}Fe spectrum, sharp peaks corresponding to the emission lines with a low energy tail. Figs. 8 and 9 show the spectra for ^{241}Am and ^{57}Co respectively. The spectra were acquired at a counting rate of about 5×10^2 counts per second. The FWHM of the peak at 59.5 keV of ^{241}Am is 332 eV while the FWHM of the peak at 122 keV of ^{57} Co is 484 eV.

The positions of the peaks of the 14 keV, 122 keV, and 136 keV lines of the ^{57}Co source and the 59.5 keV line of the ^{241}Am source give an indication of how linearly the overall system behaves. The peak positions were calculated fitting a Gaussian to the experimental spectra with the code OriginPro 8 [14]. The positions of the peaks vs. the photon energy are reported in the plot of Fig. 10 together with the straight line fit. The error on the positions estimated by the code is smaller

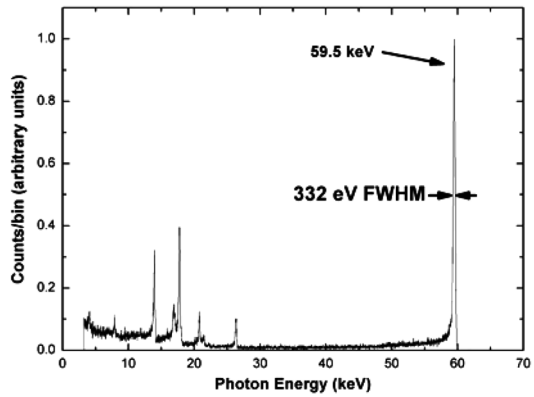

Fig. 8. Channel 10 spectrum of ^{241}Am with 10 μs shaping time. 332 eV FWHM at 59.5 keV.

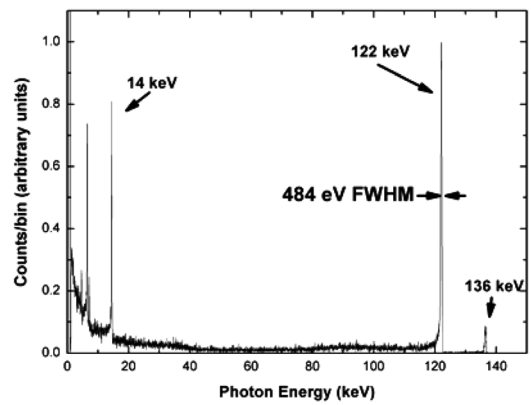

Fig. 9. Channel 10 spectrum of ^{57}Co with 10 μs shaping time. 484 eV FWHM at 122 keV.

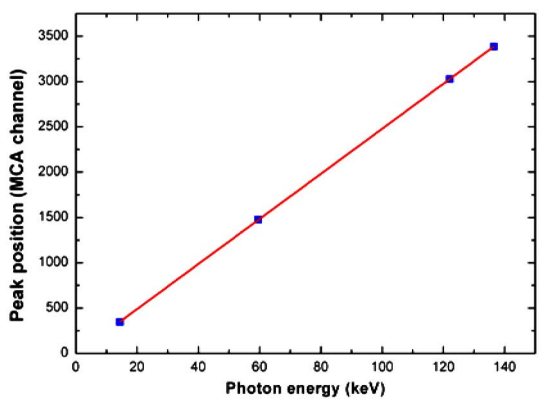

Fig. 10. Plot of the peak position in MCA channel vs. the photon energy for the 14 keV, 122 keV, and 136 keV lines of the ^{57}Co source and the 59.5 keV line of the ^{241}Am. The blue dots are the experimental points and the red line is the straight line fit. The estimated errors on the peak position are much smaller than the graphic symbol representing the data.

than 0.15 MCA channels. These errors are much smaller than the graphic symbol representing the data.

The straight line fit (slope 24.86 MCA channel/keV and offset -7.34 MCA channel) differs from the experimental points for a maximum of 4.2 MCA channels. A quadratic function fits better the experimental points; however the coefficient of the quadratic term is very small (-0.0021 MCA channel/keV^2) and the maximum deviation of the quadratic function with respect to the

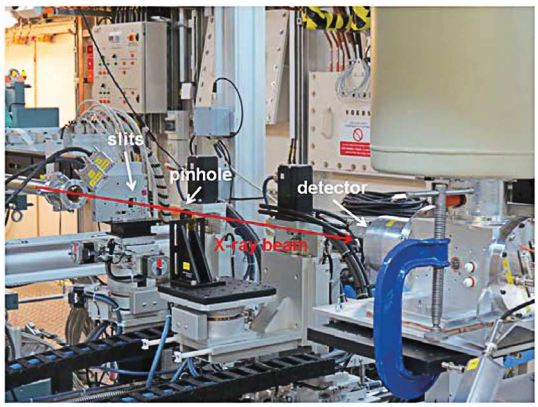

Fig. 11. The detector installed at the beam line B16. Slits, pinhole, and detector are along the X-ray path that is highlighted with a red arrow.

straight line fit is 4 MCA channel. In summary we can estimate a non-linearity of approximately 0.13%. No other sources were available in our laboratory to include more points in the plot which would provide a better estimation of the non-linearity. However this result may be limited by the accuracy of the measurements in the peak position due to thermal drifts of the electronics external to the cryostat, mainly the shaping amplifiers, as no control on the temperature was implemented.

D. Test with Synchrotron X-Ray Beam

In order to understand better the characteristics of this detector we used the X-ray beam of the test beam line, B16, of Diamond Light Source. The source of B16 is a bending magnet and it can operate with Si(111) monochromator with photon energies from 4 to 20 keV. The highly collimated and highly monochromatic beam is a very effective diagnostic tool to study detectors. The monochromatic beam can be stopped down - with slits and pinholes - to dimensions of the order of tens of microns. A map of the responsivity of the detector as a function of the beam position can then be easily produced. The effect of photons landing in the middle of a pad or close to its boundary with other pads can then be studied. Fig. 11 shows the detector installed on the beam line. The detector was located on a translational stage and had in front of it a set of slits reducing the beam to 20 μm $\times$ 20 μm followed by a 10 μm diameter pinhole in a 10 μm thick foil of tungsten. The data acquisition system used for this test consisted of a digital pulse processor manufactured by XIA LLC. The pulse processor that was used was a DXP-XMAP card [15] that enabled the acquisition of spectra of the four central channels (6, 7, 10, and 11) simultaneously. The noise performance of the detector on the beam line was not quite at the same level as during the laboratory tests and the limited time available prevented an investigation and possible solution of this problem. However this did not prevent carrying out the main task planned for this beam test which was evaluating if the low energy tail is still present when the X-ray impinges far from the pad edges and if there is any evidence of charge trapping especially at the pad edges. In order to have low harmonic content the photon energy used was 15 keV. Over 99% of 15 keV photons are absorbed in the first 100 μm of germanium [10], therefore we can expect that these spectra present similar

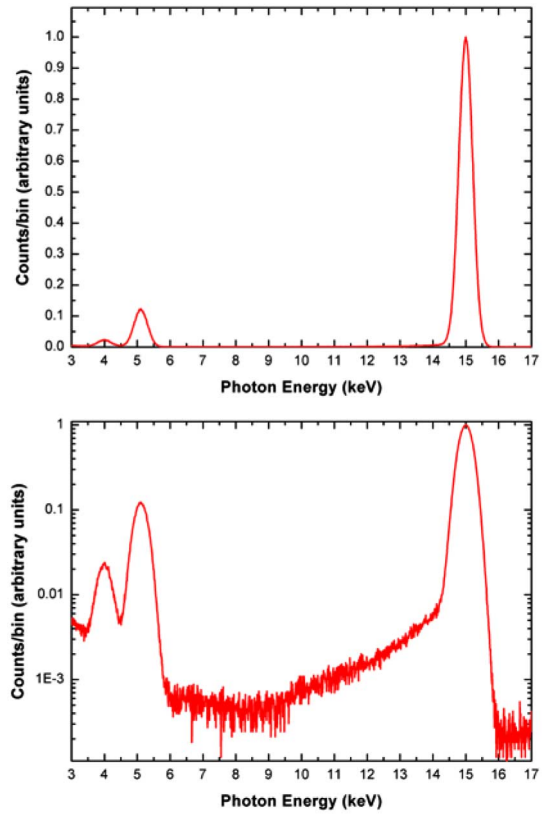

Fig. 12. Spectrum of 15 keV photons impinging in the middle of channel 10 recorded with XIA and 0.5 μs of peaking time (upper picture linear, lower picture logarithmic). The low energy tail is considerably reduced and the peak to background ratio considerably enhanced even though the energy resolution is not optimal. The two peaks around 4 and 5 keV are the germanium K_β and K_α escape peaks respectively.

features due to charge transport to those taken during the laboratory tests. Fig. 12 shows the spectra provided by the detector when the X-ray beam impinges in the middle of pad 10.

It is immediately seen that the low energy tail disappears and the peak to valley ratio is considerably enhanced. This result is the same for all the four channels tested and it is evidence that no charge is lost. This conclusion becomes still clearer when the beam is scanned across the corner of the pads 6,7,10, and 11.

The spectra from the four channels were acquired as the beam was scanned in an area of 400 μm $\times$ 400 μm with the centre as close as possible to the corner of the four pads. Fig. 13 shows three spectra of channel 6 as the beam is shifted from the left (looking at the beryllium window) towards the centre. The beam position is the nominal position provided by the motor encoders. In Fig. 13 are represented spectra for horizontal positions to -200 μm, -100 μm, and $+10$ μm. The vertical position is the same for all of the three spectra and it is $+200$ μm. The shift of the peak position reveals the fact that as the beam moves towards the edge the fraction of charge collected by the pad reduces as part of the charge is collected by the neighbour pad, in this case pad 7. The bi-dimensional map of the peak position as a function of the beam position for the four channels is shown in Fig. 14. The beam was moved in steps of 10 μm. The map is smooth with no unexpected features.

The horizontal linear profiles of the peak position of the channels 6 and 7 when the vertical position is at $+200$ μm is shown in

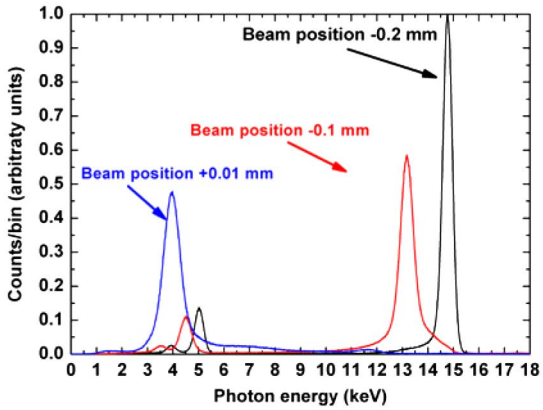

Fig. 13. Spectra of channel 6 for different horizontal beam positions. The vertical position is fixed at $+0.2$ mm.

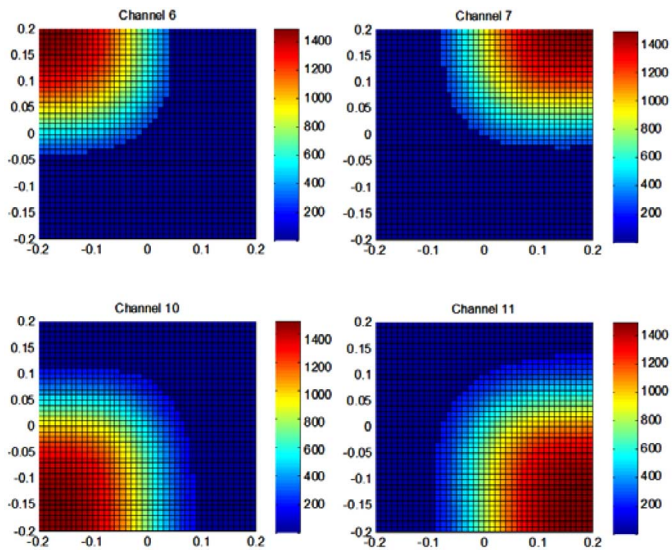

Fig. 14. Bi-dimensional map of the four channels. The plots represent the peak position in the spectrum measured by each channel as a function of the beam position. The beam position is given in mm and it is the nominal value provided by the motor encoders.

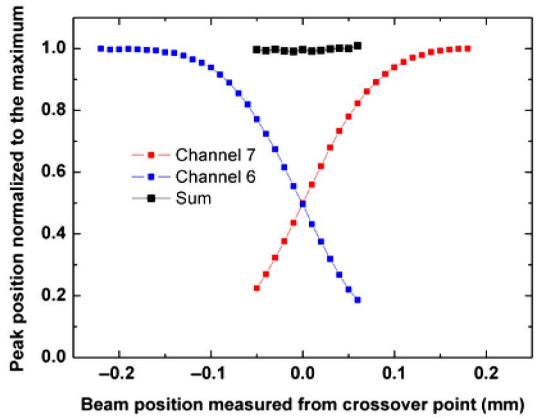

Fig. 15. Horizontal linear profiles of the peak positions of the channels 6 and 7. The peak positions are normalized to their values at the farthest position from the corner. The beam position is measured from the crossover point of the two profiles. In the graph is reported also the sum of the value of the two channels (black squares) that is very close to 1.

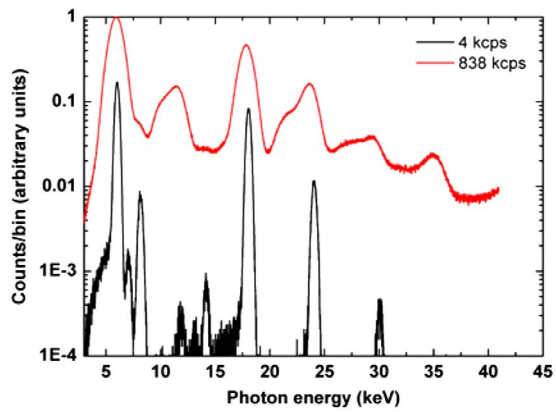

Fig. 16. Spectra of 6 keV photons and harmonics. The counting rate of the spectra shown is 4 kcps (black line) and 838 kcps (red line). The spectra are normalized to the 6 keV, 838 kcps peak. The noise counts are not shown.

Fig. 15. The peak positions are normalized to their value when the beam is at the farthest point from the corner (-200 μm for channel 6 and $+200$ μm for channel 7).

The two curves have the cross over point when the normalized peak position is 0.5. The two curves are symmetric with respect to the vertical line passing by the cross over point. If we sum the values of the two channels in the region where the curves overlap we see that the sum of the normalized peaks is very close to 1. We can then conclude that we have no evidence of charge trapping at the edges of the pads and that the low energy tail observed in the laboratory spectra are due to charge sharing only.

Another test was the measurement of the peak stability as a function of counting rate. In this case the spectra were taken at 6 keV and the counting rate changed by opening the slits. The pinhole downstream of the slits had been removed for this test. With the beam located in the centre of a pad the slits were opened from 20 μm $\times$ 20 μm to 380 μm $\times$ 380 μm. The corresponding input counting rate, as calculated by the XIA system, varied from 4 kcps to 838 kcps. The counting rate at the minimum slit aperture includes a considerable fraction of counts due to electronic noise (approximately 1.5 kcps); if this is taken into account the calculated input counting rate vs. the clear area shows a good linearity. Appropriate dead time correction models are essential for a correct linearization of the system. Fig. 16 shows the two spectra for the two counting rates in logarithmic scale. The peaking time is 2 μs for the spectrum at 4kcps and 0.5 μs for the spectrum at 838 kcps. The differences in the qualitative characteristics of the two spectra are due to the considerable pile-up happening at 838 kcps. Fig. 17 shows the plot of the peak position of the 6 keV photons as a function of counting rate. The change in the peak position is smaller than 1%. The peak stability as a function of counting rate is also a very important parameter for our application because ultimately it determines the linearity of XAFS experiments. In these experiments a discriminator window is placed around the fluorescence peak under study and the intensity of the fluorescence is calculated by counting the events happening

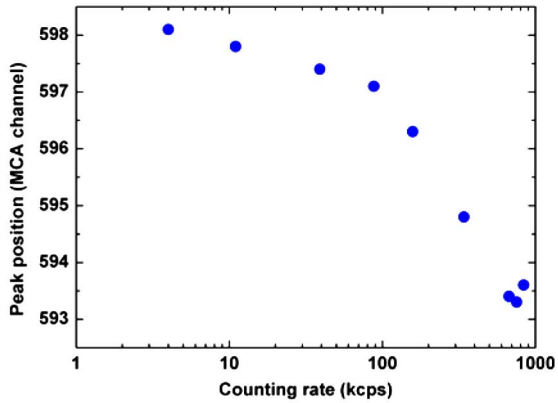

Fig. 17. 6 keV photons peak position vs. counting rate.

in the window. Drifts in the peak position lead to non-linearity of the measurement.

IV. Conclusions

The work that was presented in this paper described the characterization of a demonstrator of a spectroscopic detector system based on a monolithic multi-element germanium crystal and integrated preamplifiers. The scope of this work consisted of assessing the feasibility of this technical solution and no attempt was done to optimize the parameters of this demonstrator for its use in experiments. Nevertheless we proved that this solution for XAFS experiments is viable since this demonstrator shows that energy resolution and peak stability required by XAFS experiments can be achieved and the channel density and compactness of the system can be considerably enhanced with respect to the presently available systems.

The development of a system to be used in synchrotron experiments will require further technological advances namely in the packaging and interconnections of a considerable higher number of preamplifiers (100 or more). In addition the tail should be suppressed. This can be achieved with the use of a collimator as in the present systems. An optimization of the collimator thickness and of the pad size would be required in order to find the best trade-off between fill factor and peak to valley ratio. The development of pulse processors that can analyze pulses arriving in coincidence can be an alternative path to suppress the tail. The pulse processors will include also the appropriate calibration coefficients to equalize the gains of the channels.

Acknowledgment

The authors would like to acknowledge Diamond Light Source Ltd for funding the construction of this demonstrator and for providing beam time at the beam line B16 during the Allocation Period 14.

References

[1] G. Bunker, *Introduction to XAFS: A Practical Guide to X-ray Absorption Fine Structure Spectroscopy*. Cambridge, U.K.: Cambridge Univ. Press, 2010, 978-0-521-76775-0.
[2] D. Attwood, *Soft X-Rays and Extreme Ultraviolet Radiation*. Cambridge, U.K.: Cambridge Univ. Press, 1999, pp. 44–53.
[3] B. L. Henke, E. M. Gullikson, and J. C. Davis, "X-ray interactions: photoabsorption, scattering, transmission, and reflection at $E = 50 - 30,000$ eV, $Z = 1 - 92$," *Atom. Nucl. Data Tables*, vol. 54, pp. 181–342, 1993.
[4] J. Als-Nielsen and D. McMorrow, *Elements of Modern X-Ray Physics*. Chichester, U.K.: Wiley, 2001, p. 9.
[5] G. Derbyshire, K.-C. Cheung, P. Sangsingkeow, and S. S. Hasnain, "A low-profile monolithic multi-element Ge detector for X-ray fluorescence applications," *J. Synch. Rad.*, vol. 6, pp. 62–63, 1999.
[6] S. Diaz-Moreno, S. Hayama, M. Amboage, A. Freeman, G. Duller, and J. Sutter, "I20; the versatile X-ray absorption spectroscopy beamline at diamond light source," in *Proc. J. Physics, Conf. Series*, 2009, vol. 190, p. 012038.
[7] L. Bombelli, C. Fiorini, T. Frizzi, R. Alberti, and A. Longoni, ""CUBE", A low-noise CMOS preamplifier as alternative to JFET front-end for high-count rate spectroscopy," in *Proc. IEEE Nuclear Science Symp. Conf. Rec.*, 2011, pp. N40–5.
[8] L. Bombelli, C. Fiorini, T. Frizzi, R. Alberti, and R. Quaglia, "High rate spectroscopy with "CUBE" preamplifier coupled with silicon drift detector," in *Proc. IEEE Nuclear Science Symp. Conf. Rec.*, 2012, pp. N1–202.
[9] D. Protić and G. Riepe, "Position-sensitive germanium detectors," *IEEE Trans. Nucl. Sci.*, vol. NS-32, no. 1, pp. 553–555, Feb. 1985.
[10] Data from the Centre for X-ray Optics [Online]. Available: http://www.cxro.lbl.gov/
[11] G. De Geronimo and P. O. Connor, "MOSFET optimization in deep submicron technology for charge amplifiers," *IEEE Trans. Nucl. Sci.*, vol. 52, no. 6, pp. 3223–3232, Dec. 2005.
[12] G. Bertuccio and S. Caccia, "Noise minimization of MOSFET input charge amplifiers based on $\triangle\mu$ and $\triangle N1/f$ Models," *IEEE Trans. Nucl. Sci*, vol. 56, no. 3, pp. 1511–1520, Jun. 2009.
[13] R. G. Helmer and M. A. Lee, "Analytical functions for fitting peaks from Ge semiconductor detectors," *Nucl. Instrum. Methods*, vol. 178, pp. 499–512, 1980.
[14] [Online]. Available: http://www.originlab.com/
[15] [Online]. Available: http://www.xia.com/DXP-XMAP.html